

Modeling and Optimal Tuning of Hybrid ESS Supporting Fast Active Power Regulation of Fully Decoupled Wind Power Generators

Zhang, Chenrui; Rakhshani, Elyas; Veerakumar, Nidarshan; Rueda Torres, José Luis; Palensky, Peter

DOI

[10.1109/ACCESS.2021.3066134](https://doi.org/10.1109/ACCESS.2021.3066134)

Publication date

2021

Document Version

Final published version

Published in

IEEE Access

Citation (APA)

Zhang, C., Rakhshani, E., Veerakumar, N., Rueda Torres, J. L., & Palensky, P. (2021). Modeling and Optimal Tuning of Hybrid ESS Supporting Fast Active Power Regulation of Fully Decoupled Wind Power Generators. *IEEE Access*, *9*, 46409-46421. Article 9380359.
<https://doi.org/10.1109/ACCESS.2021.3066134>

Important note

To cite this publication, please use the final published version (if applicable).
Please check the document version above.

Copyright

Other than for strictly personal use, it is not permitted to download, forward or distribute the text or part of it, without the consent of the author(s) and/or copyright holder(s), unless the work is under an open content license such as Creative Commons.

Takedown policy

Please contact us and provide details if you believe this document breaches copyrights.
We will remove access to the work immediately and investigate your claim.

Received February 3, 2021, accepted March 8, 2021, date of publication March 17, 2021, date of current version March 30, 2021.

Digital Object Identifier 10.1109/ACCESS.2021.3066134

Modeling and Optimal Tuning of Hybrid ESS Supporting Fast Active Power Regulation of Fully Decoupled Wind Power Generators

CHENRUI ZHANG, ELYAS RAKHSHANI^{ID}, (Senior Member, IEEE),
NIDARSHAN VEERAKUMAR, JOSÉ LUIS RUEDA TORRES^{ID}, (Senior Member, IEEE),
AND PETER PALENSKY, (Senior Member, IEEE)

Department of Electrical Sustainable Energy, Delft University of Technology, 2628 Delft, Netherlands

Corresponding author: Elyas Rakhshani (rakhshani@ieee.org)

ABSTRACT The frequency stability of the power system is challenged by the high penetration of power electronic interfaced renewable energy sources (RES). This paper investigates the improvements of the frequency response of fully decoupled wind power generators (FDWG) by proposing a novel generic model implementation of ultracapacitors (UC) within a hybrid scheme in real-time simulations of wind power plants. UCs are selected as ideal power sources in fast active power-frequency control due to their high power density and fast-reacting speed. Batteries and UCs combined hybrid energy storage systems (HESS) are formed to complement their characteristics. Droop-based and frequency derivative-based control and virtual synchronous power (VSP) are the selected control strategies to support power system frequency stability. The best trade-off between frequency performance and HESS cost is found by solving a proposed optimization problem formulation. The proposed optimization problem is used to define the HESS size and the controller parameters. The optimization results show how the fast active power-frequency response is enhanced by the fast UC power injection. It also shown that VSP leads to faster frequency support than the droop-based control and the frequency derivative control.

INDEX TERMS Fast active power-frequency response, ultracapacitor model, hybrid energy storage system, fully decoupled wind power generator, mean-variance mapping optimization.

I. INTRODUCTION

Considering the sustainability and increasing electrical demands, the constitution of energy sources in the power system is changing with a trend of more renewable energy sources (RES) e.g. wind turbine generators (WTG). Traditionally, frequency stability of the power system is supported by the inertia response of conventional synchronous generators. However, the natural inertia of the wind turbine can be decoupled with the main grid when it connects through power electronic interfaces. Hence, the total amount of natural inertia can be reduced in a RES dominated power system, leading to frequency instability risks due to sudden active power imbalances [1]. To enhance the frequency stability of the power system, extra frequency control methods are required to overcome unprecedented frequency stability challenges.

The associate editor coordinating the review of this manuscript and approving it for publication was Xiaosong Hu^{ID}.

A power system with a huge amount of power electronic interfaced generation units including FDWGs has a low inertia [2]–[4], which means no direct connection exists between WTG and main grid, and no inertia from WTG is available to support system frequency. In this paper, a power system with 52% power generation from FDWGs is considered, which is simulated in real-time digital simulations (RTDS) to emulate the occurrence of fast transients. Considering the fact that the power reserve in WTG is insufficient, and adjusting the WTG rotating speed is undesirable due to technical and economic reasons [5], energy storage systems (ESS) are selected as a better power source to supply fast active power-frequency response. During a frequency disturbance, ESSs are required to supply fast active power injections in milliseconds to emulate the natural inertia response of a power system [6]. Hence, the main research question of this paper is to which extend can this fast active power-frequency response be improved.

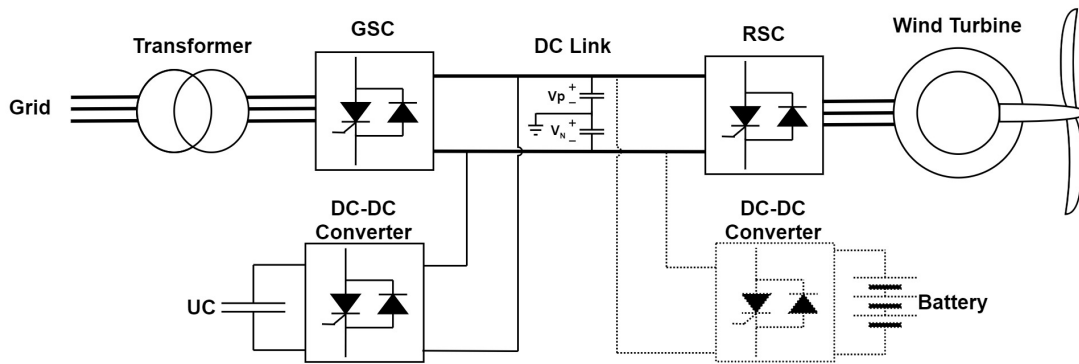


FIGURE 1. The configuration of fully decoupled wind power generator.

In [7]–[9] batteries are used as flexible energy sources to supply a bulk amount of energy is required to recover the frequency stability. However, in low inertia power systems, the changing rate-of-frequency is faster, and a battery energy storage system may not supply the power on time. An UC has higher power density and faster-reacting speed than a battery, which is ideal for performing a faster power injection. However, the energy density of UC is rather lower, and the UC price (\$/kw·h) is higher than the battery [10]. As a result, an UC and a battery-based HESS is implemented to complementarily deploy their properties.

The power allocation between UCs and batteries also influences the performance of the HESS. The UCs should supply a very fast power injection in a time scale of a few milliseconds, and the batteries are able to supply a slower long-term power. Meanwhile, a high ramp-rate of current is harmful to battery's life-time, and an UC is able to withstand a server ramp-rate of current. In specific situations, power allocation is calculated according to controller power references. In [7], the UCs emulate fast inertial response, and batteries conduct a relatively slow droop control. A high-pass filter with a cut-off frequency around 2Hz is used to allocate high-frequency power to the UCs in [11].

In this paper, a generic UC model is developed in RSCAD environment. In order to describe the fast dynamics in a time frame of milliseconds, the first contribution of this paper is building a detailed UC model in RSCAD environment to be useful for power system simulations in real-time. The fast dynamic properties of an UC are considered in this model.

In order to find the maximum improvement based on this frequency stability control strategy, the second contribution of this paper concerns with the formulation of an optimization problem, considering HESS sizing and the tuning of the parameter settings of the active power-frequency controllers. The frequency nadir and the rate-of-change-of-frequency (ROCOF) are used to describe the frequency stability performance. Hypothetically, it is considered that an improved frequency performance can be achieved with a minimized HESS cost, also taking into account that other indicators of HESS operation should be within acceptable technical performance ranges. A mean-variance mapping

algorithm (MVMO [6]) is used to solve a formulated non-convex, mixed-integer optimization problem. MVMO is a proved algorithm to solve computationally expensive (e.g. due to the solution of the differential-algebraic equation system to simulate the dynamic performance of a power system) single objective and constrained problems. A comparison of MVMO with other algorithms falls outside the scope of this paper.

The third contribution of this paper is a comprehensive analysis of the influence of optimization variables on fast active power-frequency control, especially on the improvements that can be achieved by using UCs. The performance of droop and derivative-based control and VSP are compared to illustrate the fast-reacting speed that can be achieved by using any of these methods.

The remainder of the paper is structured as follows: Section 2 presents the frequency stability control methods implemented on FDWGs. Section 3 illustrates the proposed UC model. A HESS is built in Section 4. Section 5 presents the formulation of optimization problem and provides an analysis of the results obtained by using MVMO.

II. FAST ACTIVE-POWER CONTROL STRATEGIES

A low-inertia power system with fully decoupled wind power generators is considered in this paper. Although a wind turbine contains a rotating mass, it is decoupled with the main grid by the power electronic interface. The configuration of a FDWG is shown in Fig.1. The wind turbine controllers are developed based on the IEC 61400-27 standard model [4]. The rotor-side converter (RSC) is controlled to output the maximum power generated by the wind turbine. The grid-side converter (GSC) is controlled by a voltage controller to keep DC-link voltage constant. As a result, FDWGs cannot directly support system frequency, and a power system dominated by FDWGs is vulnerable to active power imbalances.

A battery and UC combined HESS is considered as the power source for frequency stability control connecting on the DC-link of a FDWG. The battery model used for this simulation is derived from a commercial Li-ion polymer battery product TCL-PL-383562, which is a built-in model in RSCAD. The battery model is shown in the Appendix.

A buck-boost converter is used to control the power transfer between DC-link and the HESS. As the grid-side converter is set to remain the constant DC-link voltage, extra power from HESS can be delivered to the main grid and help to control the system frequency stability.

The purpose of power allocation between UCs and batteries is to achieve an operating performance according to control demands. The goal is to quickly react to control reference and extend batteries' life-time. The total HESS power is separated as a high-frequency component supplied by UC and a slow-changing component supplied by batteries. UC controllers react fast to control errors, while battery controllers generate an average value of control reference by damping out high-frequency disturbance.

A. FREQUENCY STABILITY CONTROL REQUIREMENTS

Conventionally, power system frequency is maintained 50 Hz by the rotating speed of synchronous generators. Theoretically, the synchronous speed should remain constant to ensure the healthy operation of the power system. However, the rotating speed of generators are impacted by power flows and disturbance. This phenomenon is described by the swing equation (1).

$$\frac{2H}{\omega_s} \cdot \frac{dw}{dt} = \frac{P_m - P_e}{S_b} \quad (1)$$

where H is defined as an inertia constant with second as unit; ω_s is the synchronous speed of power system; $\frac{df}{dt}$ is the rate of change of rotating speed. The right side is the power balance of a generator, where P_m is the input mechanical power from the prime mover; P_e is the output electrical power to the grid; S_b is the nominal power of a generator to transform the power into a per-unit value. The swing equation describes how the rotating speed of generator changes with power disturbance. The rotating speed w of synchronous generators will decrease when electrical power demands P_e increase, because kinetic energy stored in the rotating mass is drawn to fill the power difference. When inertia H is larger, the changing speed ω is slower, and hence the power system is more stable.

According to the swing equation, the ROCOF is defined in equation (2) as the maximum frequency gradient which is often observed around 0.5 s after an active power imbalance [7]. In equation (2), F_s is defined as the rated frequency, 50 Hz, and H_{sys} is the inertia constant of the power system. For a low-inertia power system, a frequency drop with higher ROCOF can to admissible frequency dynamics. Once an active power imbalance occurs, the minimum post-contingency frequency is defined as frequency nadir f_{nadir} in equation (3). This value is also a critical point of frequency control.

$$ROCOF = \max \left(\frac{df}{dt} \right) = \max \left(\frac{P_m - P_e}{S_b} \cdot \frac{F_s}{2H_{sys}} \right) \quad (2)$$

$$f_{nadir} = \min(f) \quad (3)$$

B. DROOP AND DERIVATIVE CONTROL

One solution is derived as derivative and droop control, which inputs frequency derivative $\frac{df}{dt}$ and frequency deviation Δf as control signals. The block diagram Fig.2 shows the configuration of droop and derivative control, where the output power reference can be represented as

$$P_{ref.droop} = \frac{1}{R} \cdot \Delta f \quad (4)$$

$$P_{ref.derivative} = \frac{2H}{F_s} \cdot \frac{df}{dt} \cdot S_b \quad (5)$$

The power reference of droop control $P_{ref.droop}$ is proportional to the frequency deviation Δf . When power output of droop control equals to the shortage of load power, the frequency deviation Δf does not increase anymore. The power reference of derivative control $P_{ref.derivative}$ comes from the swing equation (1).

An outer power controller and an inner current controller is used to generate the duty cycle to control the buck-boost converters. The input signal for power controller comes from the power error P_e . The actual power output P_m and current I_m are measure at the terminal of the HESS. The current reference for current controller is generated from the power controller. During the operation of HESS, the DC converter is basically working in buck mode, because the DC-link voltage is 4kV which is normally higher than the ESS voltage. In contrast, ESS is charged in boost mode.

The measured frequency value comes from phasor measurement units, hence the influence of frequency measurement should be taken into account. It has been proved that the PLL increases oscillations in control system [6], which is a disadvantage of droop and derivative control.

The control signal of derivative control is naturally faster than the droop control. Therefore, extra methods are not needed to separate these power references, and the control signals for UCs and batteries can be properly allocated according to this time sequence.

C. VIRTUAL SYNCHRONOUS POWER

Virtual synchronous power (VSP) is proposed under some conditions where power flows have strong relations with power system frequency. For example, one load increase leading to rising of power flows shared by synchronous generators, and this load is also supplied by RESs. When power measurements detect that the power flow from synchronous generator is rising and RES output is remaining same, this power difference is used as a signal of frequency drop according to the swing equation (1). This phenomenon inspires the idea of VSP. When a VSP is applied on a RES, the difference of power flows motivate the RES to generate more power output, which is helpful to stabilize the power system frequency. The power reference of VSP is defined as equation (6), where P_{RES} is power generation from a wind generator; P_{Bus} is the power flow delivered from the bus of the FDWG.

$$P_{ref.VSP} = P_{Bus} - P_{RES} \quad (6)$$

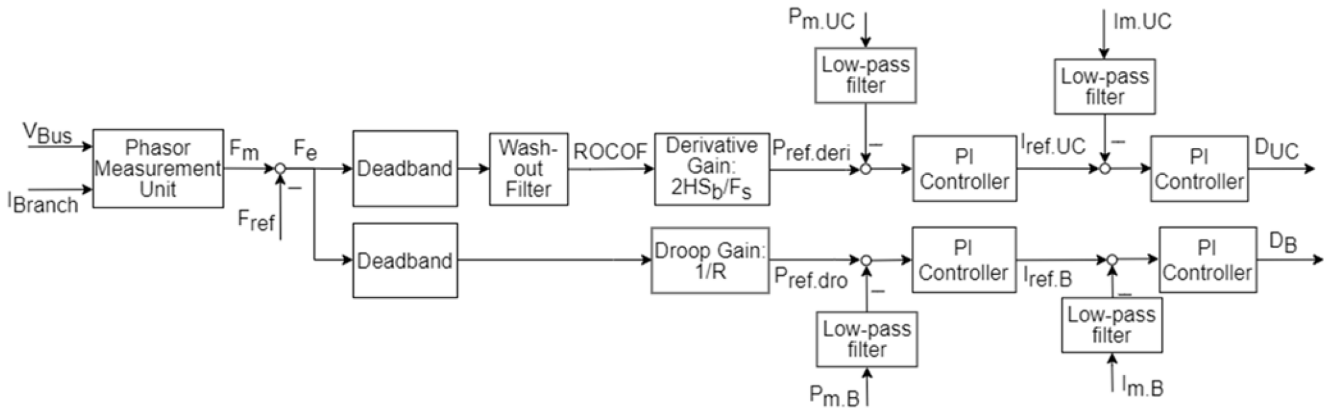


FIGURE 2. Diagram of droop and derivative control and cascaded controllers.

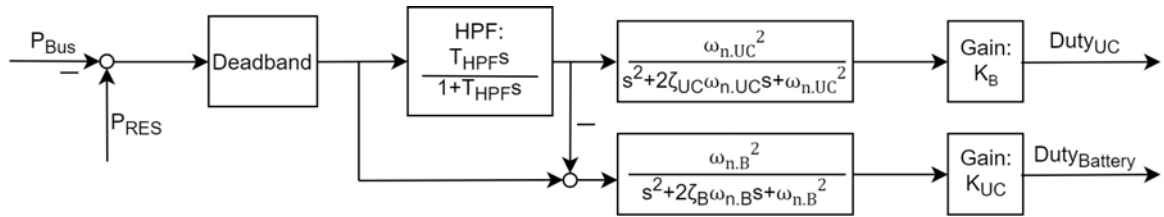


FIGURE 3. Control diagram of virtual synchronous power.

The control diagram of VSP is shown in Fig. 3. A second-order control loop is used to generate the duty cycle for DC-DC converters, where ω_n is the natural frequency and damping factor ζ . The power reference comes from the power difference. Considering a simple case of VSP application, where FDWs are connected on the same bus with synchronous generators, the power output of the common bus is the sum of total power generation. Then during the disturbance of load increase, active power is drawn from synchronous generators, and meanwhile the generation of FDWs remain constant. Due to the different power responses at FDWs and synchronous generators, the input signal of the VSP controller is not zero anymore. The power reference will force RES to increase output power and balance the power difference. The power increase is not taken from wind generators but from ESSs. The duty cycle controls the operation of interfaced power electronic converters.

A filter-based method is used to allocate the power references to UCs and batteries separately. The total power reference can be separated as fast and slow components according to a defined cut-off frequency. The ideal condition is that UCs only generate the power demand at the first one second and gradually returns to zero. However, the high-frequency disturbance from high-pass filter is easy to be amplified as oscillations in the power grid. The solution is tuning the bandwidth of UC controller. The natural frequency of the transfer function should be at least two times lower than oscillations.

Comparing with the droop and derivative-based control, VSP does not need frequency measurements. This advantage avoids the delay and instability of phasor measurement units and increases the reacting speed of frequency controllers. When system frequency changes, the angle difference still requires a time delay to be measured at the output of PLL, which slows down the reacting speed of frequency control. Instead of measuring the frequency, VSP measures the power values which changes immediately when frequency starts to change.

III. ULTRACAPACITOR MODELLING

A typical UC structure is formed by two porous electrodes, inner electrolyte and two current collectors. Fig.4 shows the inner look of a charged UC. The electrolyte is filled between the two electrodes. Therefore, the cations and anions in electrolyte are attracted by the charged electrodes. Normally, the electrodes are made of carbon with numerous pores. The attracted cations and anions distributed in the porous electrodes forming the electric potential. Comparing with parallel plat capacitors, UCs have a significantly improved the electrodes' area to $1000\text{-}2000\text{ m}^2/\text{cm}^3$ [8]. Besides, the electric filed is form between charges in porous electrodes and ions, so the small distance of electric field also increases the capacitance of UC.

A. DYNAMIC PROPERTIES OF UC

In order to build detailed UC models for fast active power-frequency response, the dynamic properties of UCs should be considered in the following three aspects.

1) DISTRIBUTED CIRCUIT ELEMENTS

Unlike in parallel plate capacitors, charges are distributed on surface of the electrodes, the porous structures of UC electrodes contain more distributed charges forming numerous particle-scale electric fields. As shown in Fig.4, the pores in electrodes are filled with electrolyte. This structure increases the effective area and decreases the distance between heterogeneous electrodes, which significantly increases the capacitance of UC. In order to model this distributed structure, partial capacitance and partial resistance need to be concerned [12].

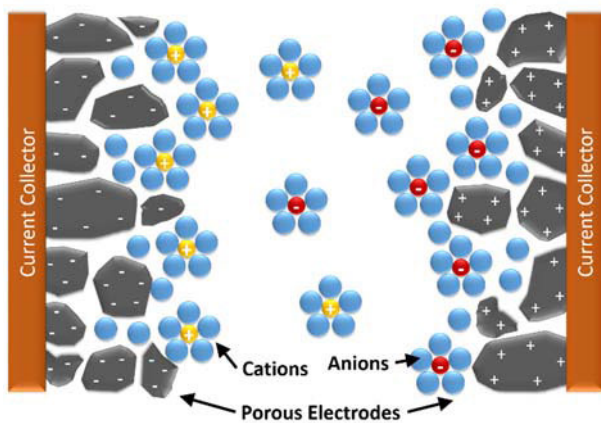


FIGURE 4. Porous structure of an ultracapacitor (inspired by [12]).

2) CHARGE REDISTRIBUTION PHENOMENON

The diffusion ions travel a time in electrolyte into the porous electrodes leading to a spontaneously changing UC voltage. Because the apparent voltage (the voltage measured between the anode and cathode) changes faster than flowing speed of ions in electrolyte. Sometimes, an UC voltage appears like fully charged, but in fact ions have not fully flowed into the pores of electrodes. If the charging current stops at this time, the apparent voltage will spontaneously decrease and show the real state of charge of the UC. For this reason, UC with same amount of stored charges can have different voltage values. When current is larger, this partial charging phenomenon is more obvious. The redistribution phenomenon can be seen as delayed currents, which can be represented by different time constants of electric circuits.

3) VOLTAGE DEPENDENCE

Experiments have proved that UC parameters are voltage and temperature dependant values [13]. In fact, an UC can be fully charged or discharged operating as an ESS in seconds [14], so UC parameters can be significantly influenced by its voltage. Meanwhile, UC parameters are also influenced by its temperature, especially in extreme environments [12]. However, the modelling of thermal environment is not the content of this paper, so the operational temperature of UCs are assumed to be perfectly controlled.

B. UC MODELLING METHODS

Considering the dynamic properties of an UC, an UC model based on different time scales is built, named as RC parallel branch model. The structure of RC parallel branch model is shown in Fig.5, where the subscripts “f”, “d” and “l” stands for fast branch (with a time constant around 20ms), delayed branch (around 100s) and long-term branch (around 30 minutes). The reason for implementing different time constants of RC branches is to represent distributed elements and charge redistribution. In steady state, capacitor voltages of three branches equal to the terminal voltage V_{UC} . When terminal voltage V_{UC} changes due to charging current I_{UC} , the voltage of fast branch capacitor C_f changes fastest to follow the terminal voltage. The delayed branch and long-term branch follow in a longer time scale, which leads to voltage differences between these branches. For this reason, the capacitor voltages will change spontaneously even when external current is removed, which corresponds to the charge redistribution phenomenon. The parameters of every branches are estimated by constant current time in different time scales. A variable capacitor shown in (7) is added on the fast branch to describe the voltage dependence of an UC, which increase the accuracy of fast UC behaviour. K_V is the voltage-dependant capacitance constant.

$$C_{var} = K_V \cdot V_{UC} \tag{7}$$

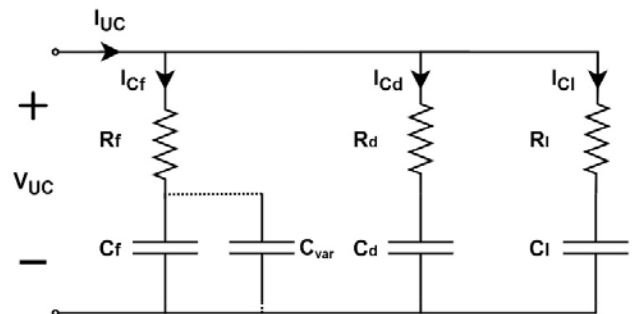


FIGURE 5. Structure of RC parallel branch model.

The selected parameter values of UC are shown in Appendix, in Table 4. In order to simulate this RC parallel branch model in RSCAD, the three RC branches are all represented as Norton form in (8), where G is the conductance value and I_{CS} is the current injection. In every simulation time step Δt , the new values for G and I_{CS} are calculated according to the terminal voltage $V_{RC}(t)$. Since three RC branches are parallel with UC terminal, $V_{RC}(t)$ equals to $V_{UC}(t)$. This is also why three branches can represent different time domains, because the charging state of every branch is independently influenced by UC voltage. Besides, the fast branch capacitance is voltage dependent, which means C_{var} needs to be updated during simulations.

$$i_{RC}(t) = G \cdot V_{RC}(t) + I_{CS}(t) \tag{8}$$

$$G = \frac{2C}{2RC + \Delta t} \tag{9}$$

$$I_{CS} = -G \cdot V_{RC}(t - \Delta t) + (2RG - 1) \cdot i_{RC}(t - \Delta t) \quad (10)$$

The charging curve of the RC parallel branch model is shown in Fig. 6(a). The testing current is shown in Fig. 6(b). The model is first charged with a constant 250A, and the terminal voltage reaches the maximum 2.424V at 1.168s. However, the ramp-rate of UC voltage is decrease with time, which shows the influence of voltage dependent capacitance. Later, during the time of zero current, the terminal voltage of UC changes spontaneously, which corresponds to the redistribution phenomenon. The ions in electrolyte are not completely located in porous electrodes during the time of charging, and the UC curve during the zero current interval shows the process of still moving ions after charging. Afterwards, UC model is discharged with a 5A current. The increasing ramp-rate of UC curve proves that UC capacitance is decreasing with voltage value. The voltage curves have step changes at the turning points, because resistors share a certain amount of voltage when current flows. Finally, the UC voltage reaches 1.218V at 4s. The UC voltage will still change in a longer time scale, but it is much longer than the time of fast active power-frequency control.

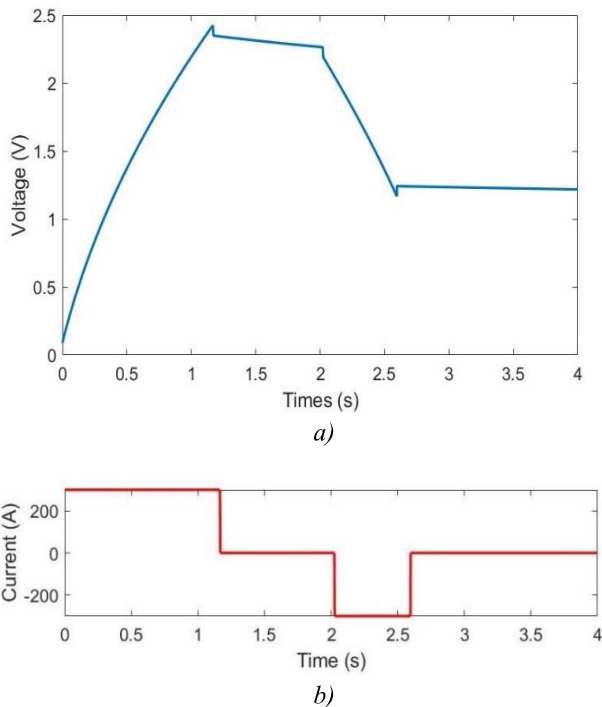


FIGURE 6. (a) Terminal voltage of UC model in RTDS, (b) Charging current for test.

IV. OPTIMIZATION FORMULATION AND NUMERICAL RESULTS

In order to find the optimal performance of HESS based frequency stability control, parameters of frequency controllers and HESS sizing is optimized in this section.

A. SETUP MODELLING FOR REAL-TIME SIMULATIONS

The 52% of power generation in IEEE 9 bus system is replaced by FDWGs at bus 7 and bus 3 as shown in Fig.7. FDWGs cannot contribute natural inertia to power system. Therefore, the system inertia is decreased, and power system frequency becomes more vulnerable to disturbance. The values of generation and loads are listed in Table 1. Wind generators are connected to power grid through back-to back converters. The RSC is controlled to transfer the maximum amount of power from wind generators. The GSC is under voltage control to maintain the DC-link voltage constant.

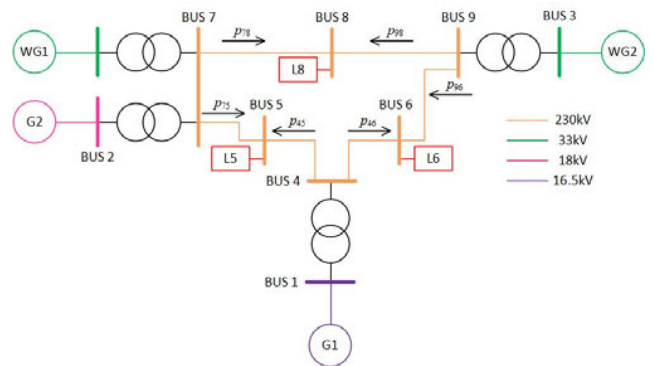


FIGURE 7. IEEE 9 bus system with 52% wind generations.

TABLE 1. Power flows in IEEE 9 bus system.

Load flow results		P (MW)	Q (Mvar)
Generations	G1	73.4	33.8
	WG1	82.6	0
	G2	78.2	-1.8
	WG2	84	0
Loads	L5	125	50
	L6	90	30
	L8	100	36

A load step increase at bus 8 is used to test the frequency stability of this power system. The scale of load increase is equal to the largest generation which is wind generation WTG2 84 MW. This load increase does not change the direction of power flows but their magnitudes. At the beginning of load increase, more active power is drawn from the rotating mass of synchronous generators, which is the reason of frequency drop. The HESSs with batteries and UCs are connected to the DC-links of FDWG located at bus 7 and bus 9 as the power sources for frequency control. The power balance of synchronous generators will be restored by increasing the power output from FDWGs.

B. FORMULATION OF THE OPTIMIZATION PROBLEM

The proposed optimization problem for controller tuning and HESS sizing takes into account four aspects: frequency stability control, the construction cost of HESS, power efficiency of HESS and high-frequency components of battery current.

The optimization problem has the following format:

$$\text{Minimize } OF(\mathbf{x}) = \text{HESS Cost} \quad (11)$$

$$\text{Subject to } g_1(\mathbf{x}) = (f_{nadir.min} - f_{nadir}) < 0 \quad (12)$$

$$g_2(\mathbf{x}) = (\text{ROCOF}_{.max} - \text{ROCOF}) < 0 \quad (13)$$

$$g_3(\mathbf{x}) = (\eta_{\text{HESS}.min} - \eta_{\text{HESS}}) < 0 \quad (14)$$

$$g_4(\mathbf{x}) = (|I_{batt.DC}|_{.min} - |I_{batt.DC}|) < 0 \quad (15)$$

The objective function $OF(\mathbf{x})$ is formulated by HESS cost, which contrasted with the obtained frequency control performance defined by the problem constraints. HESSs are the power sources selected for frequency stability control. The power capability of HESSs directly influences the performance of frequency control. However, oversized HESSs are uneconomic and unrealistic in real applications. Therefore, optimization searches for the minimal size of HESSs that fulfil frequency stability constraints.

The HESS cost can be further divided into UC cost and battery cost. The UC price and battery price are selected as 200\$/kw · h and 500\$/kw · h according to currently primary cost assumptions [2], [14]. The energy stored in one cell of fully charged battery and UC are 10404J (2.89 × 10⁻³kw · h) and 2331J (6.475 × 10⁻⁴kw · h).

Constraint g_1 is the admissible frequency nadir which is one of the frequency indicators. The admissible frequency f_{nadir} of the IEEE 9 bus system is selected as 49.2HZ according to [15]. If the frequency nadir is kept in the safe region of frequency, then the frequency stability is sufficiently protected during load disturbance.

Constraint g_2 is the upper limit of ROCOF. ROCOF describes the maximum varying speed of frequency which reflects power system inertia. As calculated in (2), ROCOF is determined by the magnitude of load change and overall inertia of the power system. When a load increase equals to the maximum generation, the upper limit of ROCOF is 0.4HZ/s as calculated in [16].

Constraint g_3 limits the efficiency of HESS η_{HESS} . A lower efficiency limit $\eta_{\text{HESS}.min}$ is selected as 0.95 according to [17]. On way is decreasing the duty cycle of buck-boost converters, which leads to a low output current and reduces the resistive losses. However, the output power is reduced. If we want to improve HESS efficiency and meanwhile increase the power output, the parallel number of HESS elements should be increased to reduce equivalent series resistance and increase the output current.

The last constraint g_4 is on the high-frequency component of battery current. A slowly changing battery current is helpful to extend batteries' life-time. In order to protect batteries from high-frequency current, frequency components of battery current should be analysed. The time domain battery current is transformed to the frequency domain to calculate the magnitude of DC component. However, there are still some magnitudes from high-frequency disturbance. The goal of 4th constraint is to limit the magnitudes of high-frequency currents. The lower threshold for the direct current

component is selected as the 75% of total current magnitudes, which stands for the majority of frequency components [18].

According to constraints and objective function, the optimization vectors for droop and derivative control \mathbf{x}_{DD} and \mathbf{x}_{VSP} are separately listed below:

$$\begin{aligned} \mathbf{x}_{DD} = [& N_{s,UC}, N_{p,UC}, N_{s,B}, N_{p,B}, K_{P,p,UC}, \\ & K_{I,p,UC}, K_{P,i,UC}, K_{I,i,UC}, K_{P,p,B}, K_{I,p,B}, \\ & K_{P,i,B}, K_{I,i,B}, H_{FDWG}, R] \end{aligned} \quad (16)$$

$$\mathbf{x}_{VSP} = [N_{s,UC}, N_{p,UC}, N_{s,B}, N_{p,B}, \omega_{n,UC}, \omega_{n,B}, \zeta_{UC}, \zeta_B, K_{UC}, K_B, T_{HPF}] \quad (17)$$

The HESS size includes the series and parallel numbers of batteries and UCs ($N_{s,UC}$, $N_{p,UC}$, $N_{s,B}$ and $N_{p,B}$).

For droop and derivative control, the power reference is calculated according to virtual inertia H_{FDWG} and frequency droop R . PI controllers are used to control the power and current of HESSs, hence the parameters of PI controllers are also chosen as optimization variables, including proportional gain and integral gain of outer power controllers of UCs ($K_{P,p,UC}$, $K_{I,p,UC}$), inner current controllers of UCs ($K_{P,i,UC}$, $K_{I,i,UC}$), same for PI controllers of batteries ($K_{P,p,B}$, $K_{I,p,B}$, $K_{P,i,B}$, $K_{I,i,B}$). These gain values should be tuned well to give a fast active-power frequency response speed and avoid noise signals in the control system.

The controllers of VSP is formed by second-order control loops. Therefore, parameters of second-order functions play an important role in reacting speed and damping noise signals. The natural frequency $\omega_{n,UC}$ and $\omega_{n,B}$, damping factors ζ_{UC} and ζ_B and gain values of second-order control loops K_B and K_{UC} should be selected. In VSP, high-pass filters are used to allocate power references, so the time constant of high-pass filter T_{HPF} is also an optimization variable.

C. MVMO ALGORITHM

MVMO is one of the promising evolutionary algorithms to tackle computationally expensive problems. It has the ability to evolve optimization variables to produce a better performance in the optimization problem. The update of optimization variables is achieved by a mean-variance mapping method. The mean value and variance of n-best optimization variables are calculated to guide the generation of new variables in the next trails, which ensures the solution evolves to the direction of better performance.

The flowchart of MVMO algorithm is shown in Fig.8. The optimization starts with randomly initialized D-dimensional variables $\mathbf{x}_0 = [\mathbf{x}_1, \mathbf{x}_2, \dots, \mathbf{x}_D]$. The values of variables are normalized between user-defined boundaries \mathbf{x}_{max} and \mathbf{x}_{min} same for the updated variables, so that variable values are always accessible and valid.

The boundaries come from sensitivity testaments as shown in Table 5. No extra constraints or penalization rules are needed to limit variables between 0 and 1.

The fitness of a set of optimization variables \mathbf{x} should be defined according to optimization problem formulated as (18). The values of frequency, ROCOF, efficiency and

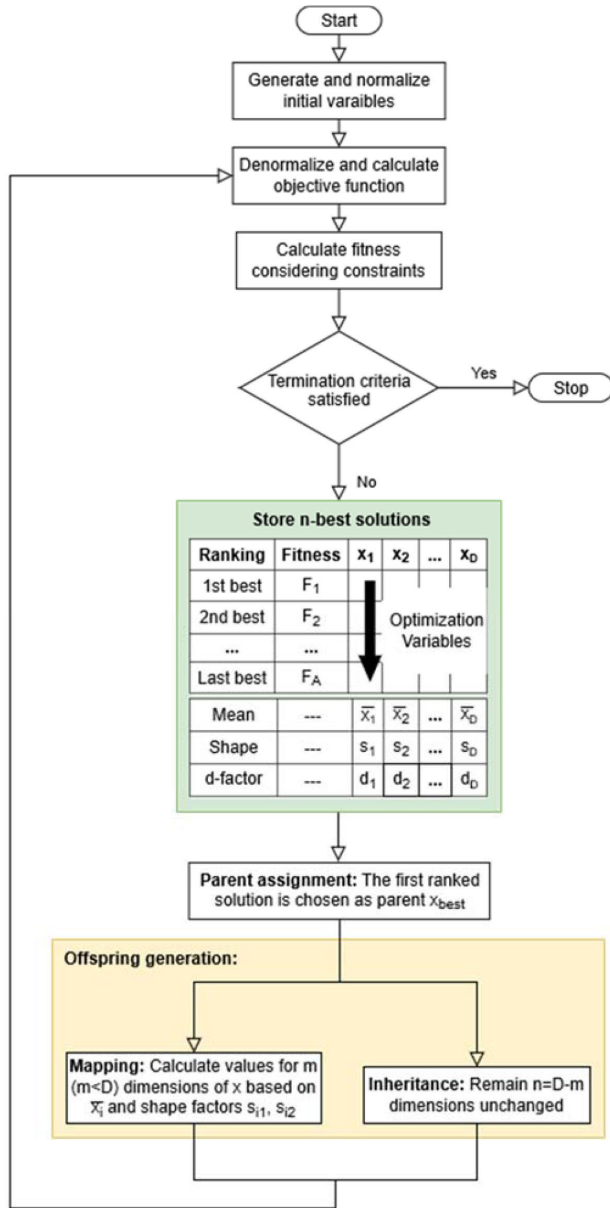


FIGURE 8. The flowchart for the MVMO algorithm procedures.

battery current should be measure during power system simulations. In every trail of optimization, new variables are used to simulate the frequency stability control results which are then evaluated by fitness values. The equation for fitness calculation is given as (18), where $OF(x)$ is the objective function value; n_{con} is the total number of constraints; λ_i is the penalty constant of i-th constraint violation; $g_{i,nor}(x)$ is the normalized value of i-th constraint, which is defined as (19). The purpose of constraint normalization is to fairly penalize constraints with different units. Comparing with the constraint penalization method with binary value, a continuous $g_i(x)$ is beneficial to the converging speed of optimization, because the latter gives the distance to the feasible solutions. The penalty of constraints are selected much larger the objective function, so that optimization algorithm will give

priority to satisfy constraints than to minimize the objective function.

$$\text{Minimize } Fitness = OF(x) - \sum_{i=1}^{n_{con}} (\lambda_i g_{i,nor}(x)) \quad (18)$$

$$g_{i,nor}(x) = \min \left[1, \max \left[\frac{g_i(x)}{g_{i,max}} \right] \right] \quad (19)$$

An archive is used to store n-best solutions during the optimization. The solutions (optimization variables) are ranked according to calculated fitness. The depth n of an archive is user-defined which influences the converging speed of optimization. Only the latest n-best solutions are stored in the archive. When a new solution x_{new} is generated with a smaller fitness than any existed solutions, it will be placed in archive according to its fitness rank comparing with other exited solutions, and the last ranked solution will be discarded from the archive. The archive keeps updating during iterations, and the optimal solution will be finally ranked at the first place. An optimization with more variables may need a larger archive. In this paper maximum 14 variables are optimized, after several testaments, the archive depth is chosen with a good convergence as 15.

The n-best solutions stored in the archive is used to generate the offspring variables x_{new} in the next iterations. The mean and variance values of n-best solutions are calculated and participate in the offspring generation to guide the mapping from parent variables x_{best} to offspring variables x_{new} . Besides, a shape factor and a d-factor are calculated according to n-best solutions and updated with iterations. The shape factor is scaling up during the optimization to increase the influence of archive members, which gives a good converging speed. The d-factor is also updating, and it oscillates around the current shape factor. The mean value, variance, shape factor and d-factor determine the mapping function from parent variables to offspring generation.

There is a dimension selection strategy before variable mutation. Not all the variables are mutated in every iteration. Instead, only m dimensions of n variables are mutated. The m dimensions of optimization variables for mapping are selected randomly before offspring generation. The other $n - m$ dimensions will remain the same as the values of the best solution x_{best} . Normally, dimension m gradually decreases from a large initial value during optimization. Consequently, more dimensions of optimization variables are mutated at the beginning, and later, only several non-optimal dimensions of variables are selected for mapping. The benefit of this strategy is increasing the converging speed of optimization.

The MVMO code is written in MATLAB scripts. However, the real-time simulation of the IEEE 9 bus system is processed in RSCAD every iteration. Therefore, communication channels between MATLAB and RSCAD should be established in every iteration to exchange new optimization variables and simulation results. The communication channel between MATLAB and RSCAD is established by using command 'ListenOnport()'. This command establish a TCP/IP

socket communication between RSCAD and MATLAB and makes RSCAD 'Runtime' file listen to the commands from MATLAB. First, MATLAB assigns new optimization variables to the IEEE 9 bus system model in RSCAD and compile it. Then, RSCAD is commanded to start the simulation and record the plots of results. Finally, simulation is stopped and the communication channel is closed by MATLAB.

D. OPTIMIZATION RESULTS

After 300 fitness evaluations, the optimization results give the optimal solutions of two cases with minimized fitness values. The convergence of optimization can be shown by the fitness curves during evaluations in Fig.9. The fitness value has been normalized to its initial value as equation (20). Because the initial value is also the largest fitness value, and the fitness value is gradually reduced during optimization.

$$\text{Normalized Fitness} = \frac{\text{Fitness}}{\text{Fitness}(1)} \quad (20)$$

Fig. 9(a) shows the fitness evaluations and objective function values of droop and derivative control during the optimization. The optimization starts with a random initial state, and fitness value is rather high at the beginning which is due to violation of some constraints.

The fitness converges fast in the first 100 iterations, which means constraints are gradually satisfied during this time. Afterwards, fitness is slightly improved by decreasing the value of the objective function. Meanwhile, the value of the objective function is also higher at the beginning, because the HESS is oversized. Then the cost of HESS is reduced during the optimization, and finally, the optimal solution gives a minimized HESS cost.

Fig. 9(b) shows the convergence of optimization variables. These variables are normalized within the upper and lower boundaries as shown in Table 5.

The real values of the optimal solution are shown in Table 6. Optimization starts with random initial values which violate many optimization constraints leading to a high fitness value. The variable values oscillate a lot to search for satisfied solutions before 100 iterations. Later, variable values gradually converge to the solution that MVMO algorithm found. The integral gain value for UC $K_{I,i,UC}$ is obviously larger than battery value $K_{I,i,B}$, because UC current is faster than battery.

Similar phenomenon of fitness, objective function and optimization variables in VSP case can be observed in Fig.10. The values of optimization variables are shown in Table 7. The normalized fitness also converges fast before 100 iterations, but its final value 0.0109 is much lower than droop and derivative control case value 0.128. Because the fitness is normalized by its initial value which has a larger difference in two cases.

More constraints are violated at the beginning of VSP optimization (penalty 3.16×10^7) than droop and derivative control case (penalty 2.73×10^6) leading to a smaller normalized VSP fitness. In fact, the fitness values in both cases

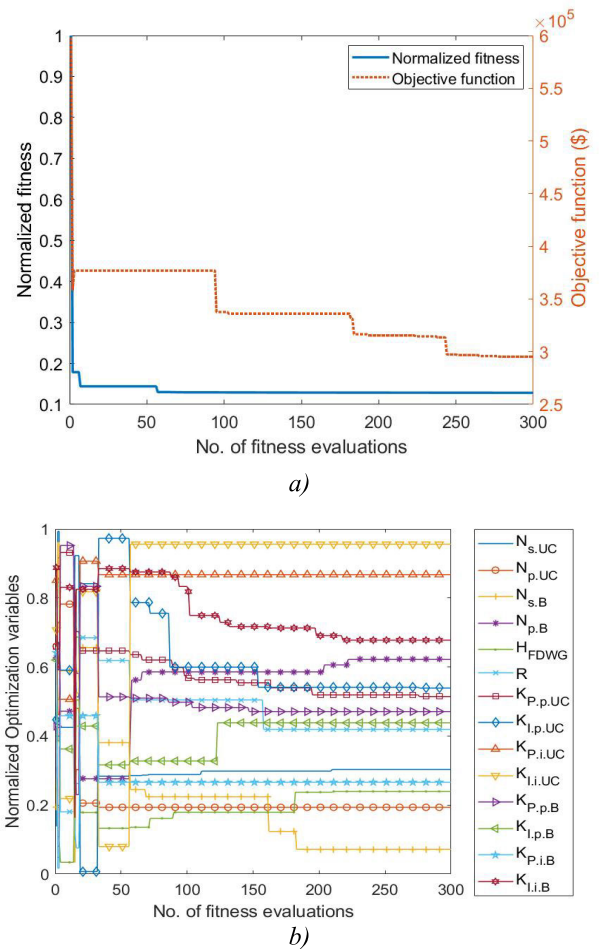


FIGURE 9. (a) Normalized fitness value and objective function value, and (b) normalized optimization variables of droop and derivative control.

are finally optimized to the same level. The oscillation of objective function shown in Fig. 10(a) takes a longer time to converge comparing with droop and derivative control optimization, which means constraints take longer time to be fully satisfied. This oscillation is also reflected in the variation of optimization variables in Fig. 10(b). After the oscillation, variable values are very close to the optimal solution and gradually converge to it.

The results of frequency stability control before and after the optimization of droop and derivative control are compared in Fig. 11(a). The critical values are listed in Table2. The previous setting of frequency stability control is set just above admissible frequency 49.2 Hz in an 84 MW load increase condition, and ROCOF is controlled around 0.4 Hz/s. However, this performance is achieved according to the lowest standard, and the battery efficiency 0.9057 is lower than the required efficiency 0.95. After the optimization, as shown in Table2, the settled frequency is significantly improved with a nadir of 49.5931Hz. The rising of settled frequency is because of the optimally tuned frequency droop and HESS size. It is worth to mention, although the settled frequency may increase with the droop setting, it is still limited by the power capability

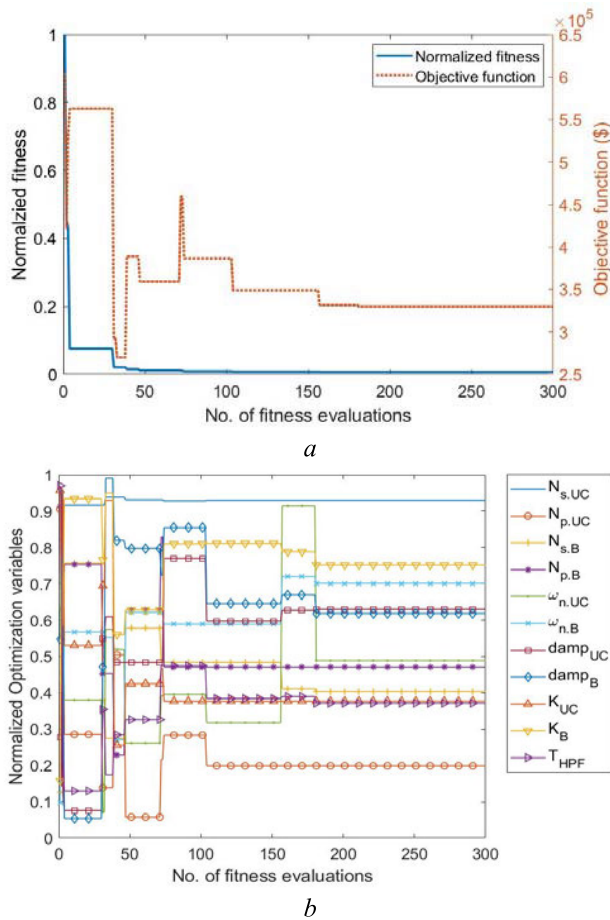


FIGURE 10. (a) Normalized fitness value and objective function value, and (b) normalized optimization variables of VSP.

of HESS. That is why HESS size and frequency droop is optimized together.

The power output of frequency stability control is shown in Fig. 11(d). The UC power after optimization is faster and larger than the previous value, because UCs are sized larger, and PI controller for UC is tuned faster. Since the droop setting is increased, the battery power output is around 10MW larger than the previous result.

Considering the construction cost of HESS, the battery cost is increased due to the expansion of parallel cells. After increasing the parallel number $N_{p,B}$, the equivalent series resistance of batteries is reduced and optimized efficiency of power delivery is improved to 0.9699. The cost of UCs does not change much, which means the previous UC size is sufficient to supply the required power. Since UCs have a very low equivalent series resistance, UC efficiency η_{UC} is not a problem. Fig. 11(b) shows the frequency curve of VSP before and after optimization. As shown in Table3, the optimized ROCOF is reduced 0.08HZ/s than the old value. Hence, the frequency is settled earlier after optimization, which means the power difference between FDWG generations and the power flows delivered by FDWGs located buses 7 and 9 to load 8 (P_{7-8} and P_{9-8}) is balanced faster. According to swing

TABLE 2. Comparison of droop and derivative control results.

	Without optimization	With optimization
f_{nadir}	49.5517HZ	49.6908HZ
ROCOF	0.3844HZ/s	0.3045HZ/s
$N_{s,UC}$	1200	698
$N_{p,UC}$	200	551
$N_{s,B}$	900	866
$N_{p,B}$	300	410
UC cost	77700\$	124510\$
Battery cost	156060\$	205230\$
Total HESS cost	233760\$	329740\$
η_{UC}	0.9939	0.9846
$\eta_{battery}$	0.8897	0.9591

TABLE 3. Comparison of VSP results.

	Without optimization	With optimization
f_{nadir}	49.5517HZ	49.6908HZ
ROCOF	0.3844HZ/s	0.3045HZ/s
$N_{s,UC}$	1200	698
$N_{p,UC}$	200	551
$N_{s,B}$	900	866
$N_{p,B}$	300	410
UC cost	77700\$	124510\$
Battery cost	156060\$	205230\$
Total HESS cost	233760\$	329740\$
η_{UC}	0.9939	0.9846
$\eta_{battery}$	0.8897	0.9591

equation (1), frequency drop is prevented after power balance. Therefore, faster controller response is one reason to explain why VSP has a higher settled frequency after optimization. The other reason is the increased controller gain values K_{UC} and K_B which determine the controller sensitivity to input signals. A higher gain means a smaller settling error of input power difference.

As shown in Fig. 11(e), the power output after optimization is 10 MW larger than the old value, which can explain why frequency is settled at a higher value after optimization. After optimization, more load demand is undertaken by HESSs leading to a higher settled frequency. The optimized UC power is also faster and higher than the old curve. The higher power reference from the frequency controller needs to be supplied by a larger size of UCs. However, high gain values are not always suitable in VSP controllers. Since the output signal of the VSP controller is duty cycle which is only valid between 0 and 1, a large gain value may saturate the duty cycle, especially when the power capacity of HESS is insufficient. The frequency analysis of battery current shows that the 75% of current magnitudes are located at the left side of the red line 3.8983 Hz. As the DC component of battery current is added in constraint $g_4(x)$, the oscillation

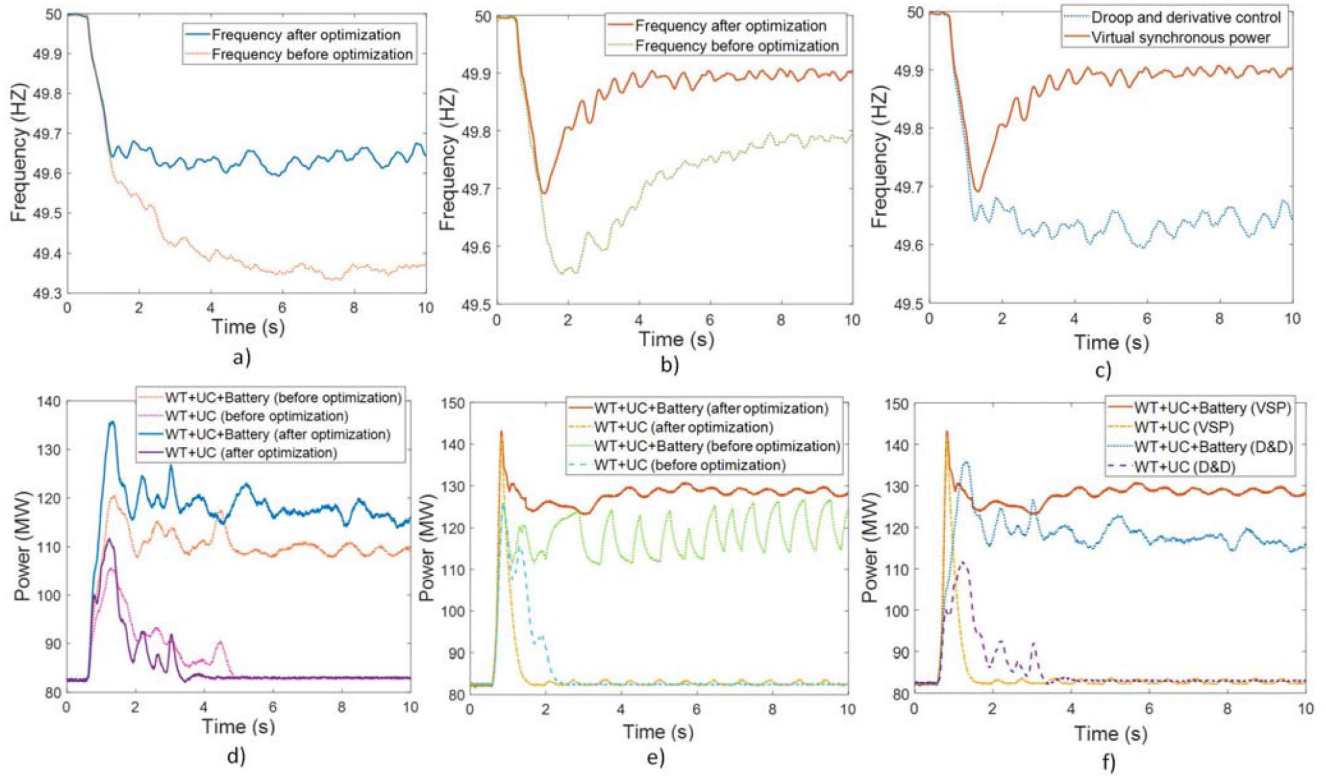


FIGURE 11. (a) Frequency of droop and derivative control before and after optimization, (b) Frequency of VSP before and after optimization, (c) Optimized frequency of droop and derivative control and VSP, (d) Power output of droop and derivative control before and after optimization, (e) Power output of VSP before and after optimization, (f) Power output of optimized droop and derivative control and VSP.

magnitude after optimization is damped a lot. The position of 75% of current magnitude is improved to 1.399 Hz. As a result, the oscillation in battery current is sufficiently avoided.

The frequency of droop and derivative control and VSP is compared in Fig. 11(c). VSP obviously has a better frequency nadir and ROCOF. The reason for this better performance can be explained by the power output of two cases in Fig. 11(f). The generation of wind turbine can be assumed constant during the time of frequency disturbance. Then the curves above 82 MW can be seen as the extra power generation from HESSs.

ROCOF is mainly influenced by UC power. The derivative control requires frequency measurement and derivative calculation. As observed from the corresponding curve, the UC output of derivative control works in around 3 seconds from beginning. For VSP, UCs operate in around 1 second from the beginning. The UC output in VSP is larger and faster than derivative control leading to a lower ROCOF, which can be explained by VSP principles. Since VSP does not need frequency measurement and derivative calculation, VSP is able to avoid the delay and disturbance caused by frequency measurement. As observed, UCs of VSP reach the peak value earlier than derivative control case, the UC power equals the total power for 1s in VSP case. Besides, the power reference of UC in VSP comes from a HPF, which means UCs can

immediately supply a step power increase. Comparing with derivative control, VSP can make a better use of the high power density of UCs.

The battery power output gradually increases to replace the UC power. For droop control, battery power completely replaces UC when frequency reached the set frequency around 4s. In contrast, VSP is trying to fill the power gap between FDWG generation and the power delivered from the FDWG connected bus. Comparing with final battery output power of droop control, battery output of VSP is around 10MW larger. Because the power output of droop control is settled when the frequency is stabilized. In contrast, after stabilising the system frequency, VSP still needs to catch up the changing of mentioned power difference. From swing equation point of view, droop control aims to achieve P_e equals to P_m at synchronous generators, while VSP aims to recover the P_e as the original value. This can also explain why the HESS of VSP is sized larger than HESS of droop and derivative control.

V. CONCLUSION

Fast dynamic properties including distributed circuit elements, internal redistribution phenomenon and voltage dependent impedance are considered for a generic UC modeling as proposed in this paper with real-time simulation cases.

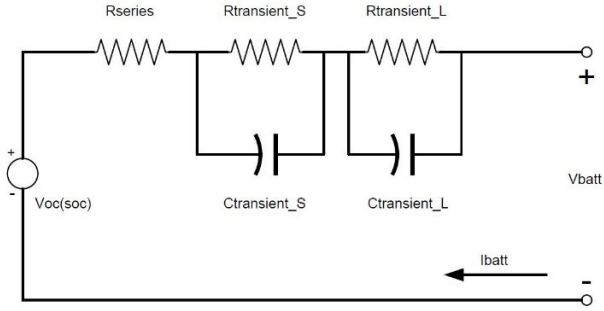


FIGURE 12. Structure of battery model.

TABLE 4. UC model parameters.

C_f :	270F	R_f :	2.5mΩ
C_d :	100F	R_d :	0.9Ω
C_i :	220F	R_i :	5.2Ω
K_V :	190F/V		

TABLE 5. Upper and lower limits of optimization variables.

Variable	Min	Max	Variable	Min	Max
$N_{s,UC}$	174	1739	$K_{I,i.B}$	0.0	10.0
$N_{p,UC}$	1	884	$H_{FDWG}(s)$	10.0	25.0
$N_{s,B}$	118	1176	$R(HZ/MW)$	0.05	0.3
$N_{p,B}$	1	1196	$\omega_{n,UC}(rad/s)$	0.0	120.0
$K_{P,p,UC}$	0.0	1.0	$\omega_{n,B}(rad/s)$	0.0	120.0
$K_{I,p,UC}$	0.0	10.0	ζ_{UC}	0.0	1.2
$K_{P,i,UC}$	0.0	1.0	ζ_B	0.0	1.2
$K_{I,i,UC}$	0.0	20.0	K_{UC}	0.0	1.0
$K_{P,p,B}$	0.0	1.0	K_B	0.0	1.0
$K_{I,p,B}$	0.0	10.0	$T_{HPF}(s)$	0.0	0.6
$K_{P,i,B}$	0.0	1.0			

In order to describe these properties in real-time simulations, a RC parallel branch model is represented in RSCAD environment. This UC model is combined with a battery model to simulate a HESS in RTDS, which takes the high power density of UC and high energy density of the battery.

An optimization of HESS sizing and controller parameter tuning is formulated to find the best frequency performance until a minimized HESS size. The optimization results show that the frequency control performance can be significantly improved by injecting fast power from UCs. Therefore, UCs are sized larger to increase the power capability of the HESSs. Meanwhile, controllers, especially for UC controllers, are tuned to react faster to power references. The parallel number of batteries are increased to meet the efficiency constraint.

Comparing the optimal performance of droop and derivative control and VSP, VSP supplies a faster active power response, because the power reference of VSP comes from a power difference which avoids the delay of frequency measurement. Meanwhile, UCs are sized larger in VSP case to supply a larger magnitude of power. The faster and higher UC power in VSP shows that the fast power reference of VSP can

TABLE 6. Optimal solution of droop and derivative control.

$N_{s,UC}$:	886	$K_{P,i,UC}$:	10.10
$N_{p,UC}$:	266	$K_{P,p,B}$:	0.56
$N_{s,B}$:	545	$K_{I,p,B}$:	6.02
$N_{p,B}$:	695	$K_{P,i,B}$:	0.18
$K_{P,p,UC}$:	0.77	$K_{P,i,B}$:	3.27
$K_{I,p,UC}$:	6.57	H_{FDWG} :	22.41s
$K_{P,i,UC}$:	0.58	R :	0.012HZ/MW

TABLE 7. Optimal solution of VSP.

$N_{s,UC}$:	698	ζ_{UC} :	0.50
$N_{p,UC}$:	551	ζ_B :	0.65
$N_{s,B}$:	866	K_{UC} :	0.65
$N_{p,B}$:	410	K_B :	0.79
$\omega_{n,UC}$:	36.82rad/s	T_{HPF} :	1.72s
$\omega_{n,B}$:	65.44rad/s		

TABLE 8. Battery model parameters.

V_{OC} :	$-1.031 \cdot e^{-35 \cdot SOC} + 3.685 + 0.2156 \cdot SOC - 0.1178 \cdot SOC^2 + 0.3201 \cdot SOC^3$
R_{series} :	$0.1562 \cdot e^{-24.37 \cdot SOC} + 0.07446$
$R_{Transient_S}$:	$0.3208 \cdot e^{-29.14 \cdot SOC} + 0.04669$
$C_{Transient_S}$:	$-752.9 \cdot e^{-13.51 \cdot SOC} + 703.6$
$R_{Transient_L}$:	$6.603 \cdot e^{-155.2 \cdot SOC} + 0.04984$
$C_{Transient_L}$:	$-6056 \cdot e^{-27.12 \cdot SOC} + 4475$

make a better use of the advantages of UCs. Future work will be devoted to apply the proposed UC model and optimization problem formulation in other types of decoupled renewable generation and also in responsive demand.

APPENDICES

See Figure 12.

See Table 4, 5, 6, 7, 8.

REFERENCES

- [1] S. M. Alhejaj and F. M. Gonzalez-Longatt, "Investigation on grid-scale BESS providing inertial response support," in *Proc. IEEE Int. Conf. Power Syst. Technol. (POWERCON)*, Sep. 2016, pp. 125–138.
- [2] H. Mortazavi, H. Mehrjerdi, M. Saad, S. Lefebvre, D. Asber, and L. Lenoir, "A monitoring technique for reversed power flow detection with high PV penetration," *IEEE Trans. Smart Grid*, vol. 6, no. 5, pp. 2221–2232, Sep. 2015.
- [3] A. Adrees, J. V. Milanović, and P. Mancarella, "Effect of inertia heterogeneity on frequency dynamics of low-inertia power systems," *IET Gener., Transmiss. Distrib.*, vol. 13, no. 14, pp. 2951–2958, Jul. 2019.
- [4] S. Engelken, A. Mendonca, and M. Fischer, "Inertial response with improved variable recovery behaviour provided by type 4 WTs," *IET Renew. Power Gener.*, vol. 11, no. 3, pp. 195–201, Feb. 2017.
- [5] J. Zhu, J. Hu, W. Hung, C. Wang, X. Zhang, S. Bu, Q. Li, H. Urdal, and C. D. Booth, "Synthetic inertia control strategy for doubly fed induction generator wind turbine generators using lithium-ion supercapacitors," *IEEE Trans. Energy Convers.*, vol. 33, no. 2, pp. 773–783, Jun. 2018.

- [6] E. Rakhshani and P. Rodriguez, "Inertia emulation in AC/DC interconnected power systems using derivative technique considering frequency measurement effects," *IEEE Trans. Power Syst.*, vol. 32, no. 5, pp. 3338–3351, Sep. 2017.
- [7] J. Fang, Y. Tang, H. Li, and X. Li, "A battery/ultracapacitor hybrid energy storage system for implementing the power management of virtual synchronous generators," *IEEE Trans. Power Electron.*, vol. 33, no. 4, pp. 2820–2824, Apr. 2018.
- [8] M. P. N. van Wesenbeeck, S. W. H. de Haan, P. Varela, and K. Visscher, "Grid tied converter with virtual kinetic storage," in *Proc. IEEE Bucharest PowerTech*, Jun. 2009, pp. 1–7.
- [9] J. Rocabert, R. Capo-Misut, R. S. Munoz-Aguilar, J. I. Candela, and P. Rodriguez, "Control of energy storage system integrating electrochemical batteries and supercapacitors for grid-connected applications," *IEEE Trans. Ind. Appl.*, vol. 55, no. 2, pp. 1853–1862, Mar. 2019.
- [10] I. Mathews, B. Xu, W. He, V. Barreto, T. Buonassisi, and I. M. Peters, "Techno-economic model of a second-life energy storage system for utility-scale solar power considering li-ion calendar and cycle aging," 2020, *arXiv:2003.03216*. [Online]. Available: <http://arxiv.org/abs/2003.03216>
- [11] B. Hredzak, V. G. Agelidis, and G. D. Demetriades, "A low complexity control system for a hybrid DC power source based on ultracapacitor–lead–acid battery configuration," *IEEE Trans. Power Electron.*, vol. 29, no. 6, pp. 2882–2891, Jun. 2014.
- [12] S. Atcitty, "Electrochemical capacitor characterization for electric utility applications," Ph.D. dissertation, Dept. Elect. Comput. Eng., Virginia Tech, Chennai, India, 2006.
- [13] C.-J. Chiang, J.-L. Yang, and W.-C. Cheng, "Temperature and state-of-charge estimation in ultracapacitors based on extended Kalman filter," *J. Power Sources*, vol. 234, pp. 234–243, Jul. 2013.
- [14] A. A. Akhil, *DOE/EPRI 2013 Electricity Storage Handbook in Collaboration With NRECA*. Albuquerque, NM, USA: Sandia National Laboratories Albuquerque, 2013.
- [15] V. Knap, R. Sinha, M. Swierczynski, D.-I. Stroe, and S. Chaudhary, "Grid inertial response with lithium-ion battery energy storage systems," in *Proc. IEEE 23rd Int. Symp. Ind. Electron. (ISIE)*, Jun. 2014, pp. 1817–1822.
- [16] M. Altin, R. Teodorescu, B. B. Jensen, U. D. Annakkage, F. Iov, and P. C. Kjaer, "Methodology for assessment of inertial response from wind power plants," in *Proc. IEEE Power Energy Soc. Gen. Meeting*, Jul. 2012, pp. 1–8.
- [17] C. Zhao, H. Yin, and C. Ma, "Equivalent series resistance-based real-time control of battery-ultracapacitor hybrid energy storage systems," *IEEE Trans. Ind. Electron.*, vol. 67, no. 3, pp. 1999–2008, Mar. 2020.
- [18] D. B. W. Abeywardana, B. Hredzak, V. G. Agelidis, and G. D. Demetriades, "Supercapacitor sizing method for energy-controlled filter-based hybrid energy storage systems," *IEEE Trans. Power Electron.*, vol. 32, no. 2, pp. 1626–1637, Feb. 2017.



include optimal power flow optimization, power system frequency control, and power system modeling.



After that he joined ABB power grid in 2020 and HESStec, Spain, in

CHENRUI ZHANG was born in 1996. He received the B.Sc. degree in electrical engineering and automation from Beijing Forestry University, China, in 2018, and the M.Sc. degree in electrical engineering tracking electrical power engineering from the Delft University of Technology, Netherlands, in 2020. During this time, he specialized in smart AC and DC grids. He is currently a Researcher with the CSG Electric Power Research Institute, Guangzhou, China. His research interests

ELYAS RAKHSHANI (Senior Member, IEEE) was born in 1982. He received the Ph.D. degree (*cum laude*) in electrical engineering from the Technical University of Catalonia (UPC), Barcelona, Spain, in 2016. From 2013 to 2016, he joined the Research Department, ABENGOA Company, Seville, Spain, as a Junior Researcher, working on different projects related to modern power systems. Since March 2017, he has been with the IEPG Center, Delft University of Technology, The Netherlands, working on European projects related to control and dynamic stability assessment of renewable/power electronic based power grids. After that he joined ABB power grid in 2020 and HESStec, Spain, in

2021, as a Senior Consultant and a Technical Manager, respectively. He is responsible for different work packages in national and European projects focused on development of hybrid energy storage system (HESS), and power and energy management systems (PMS&EMS) for providing grid functionalities. His research interests include power system control and dynamics, renewables and power converter integration, energy storage integration, frequency control, and optimal intelligent control. On the basis of his research, he published and presented several scientific works/papers in the most distinguished journals and international conferences in the electrical engineering. In 2019, he received the Extraordinary Doctorate Awards from the UPC. He served as a Reviewer for various journals and IEEE conferences. He also served as the Technical Program Committee (TPC) Member for different. He is serving as an Associate Editor for several journals, such as IEEE SYSTEMS JOURNAL and *IET Generation, Transmission and Distribution* and a Deputy Subject Editor for *IET Renewable Power Generation* Journal.



JOSÉ LUIS RUEDA TORRES (Senior Member, IEEE) was born in 1980. He received the Diploma degree (*cum laude*) in electrical engineer from Escuela Politécnica Nacional, Quito, Ecuador, in August 2004, and the Ph.D. degree in electrical engineering from the National University of San Juan, in November 2009, obtaining the highest mark 'Sobresaliente' (Outstanding). From September 2003 to February 2005, he worked in Ecuador, in the fields of industrial control systems and electrical distribution networks operation and planning. From August 2010 to February 2014, he worked as a Postdoctoral Research Associate with EAN. He is currently an Associate Professor leading the research team on stability, control, and optimization, within the Intelligent Electrical Power Grids Section, Department of Electrical Sustainable Energy, Delft University of Technology, Delft, Netherlands. His research interests include stability and control of power systems and multi-energy systems, power system operational planning and reliability, and probabilistic and artificial intelligence methods. He is currently a member of the Technical Committee on Power and Energy Systems of International Federation of Automatic Control (IFAC), the Chairman of the IEEE PES Working Group on Modern Heuristic Optimization, a Secretary with CIGRE JWG C4/C2.58/IEEE Evaluation of Voltage Stability Assessment Methodologies in Transmission Systems, a Secretary with the IEEE PES Intelligent Systems Subcommittee, and a Vice-Chair of the IFAC Technical Committee TC 6.3. Power and Energy Systems on Social Media.



PETER PALENSKY (Senior Member, IEEE) was born in Austria, in 1972. He received the M.Sc. degree in electrical engineering and the Ph.D. degree from the Vienna University of Technology, Austria, in 1997 and 2001, respectively. After that, he co-founded an Envidatec, a German startup on energy management and analytics. He joined the Lawrence Berkely National Laboratory, CA, USA, as a Researcher, and the University of Pretoria, South Africa, in 2008. In 2009, he became the Head of the business unit on sustainable building technologies with the Austrian Institute of Technology (AIT), and later the First Principle Scientist of Complex Energy Systems with AIT. In 2014, he was appointed as a Full Professor of Intelligent Electric Power Grids with TU Delft. His main research interests include energy automation networks, smart grids, and modeling intelligent energy systems. He is active in international committees, like ISO or CEN. He serves as an IEEE IES AdCom member-at-large in various functions for the IEEE. He is the Editor-in-Chief of *IEEE Industrial Electronics Magazine*, an Associate Editor of the several other IEEE publications, and regularly organizes the IEEE conferences.

...